Heat Mass Transfer (2015) 51:1779–1790
DOI 10.1007/s00231-015-1532-4

ORIGINAL

Thermo-mechanical analysis of an internal cooling system with various configurations of a combustion liner after shell

Hokyu Moon[1] · Kyung Min Kim[2] · Jun Su Park[3] · Beom Seok Kim[1] · Hyung Hee Cho[1]

Received: 29 April 2014 / Accepted: 2 March 2015 / Published online: 29 March 2015

Abstract The after-shell section, which is part of the gas turbine combustion liner, is exposed to the hottest combustion gas. Various cooling schemes have been applied to protect against severe thermal load. However, there is a significant discrepancy in the thermal expansion with large temperature differences, resulting in thermo-mechanical crack formation. In this study, to reduce combustion liner damage, thermo-mechanical analysis was conducted on three after-shell section configurations: inline-discrete divider wall, staggered divider wall, and swirler wall arrays. These array components are well-known heat-transfer enhancement structures in the duct. In the numerical analyses, the heat transfer characteristics, temperature and thermo-mechanical stress distribution were evaluated using finite volume method and finite element method commercial codes. As a result, we demonstrated that the temperature and the thermo-mechanical stress distribution were readily dependent on the structural array for cooling effectiveness and structural support in each modified cooling system. Compared with the reference model, the swirler wall array was most effective in diminishing the thermo-mechanical stress concentration, especially on the inner ring that is vulnerable to crack formation.

✉ Hyung Hee Cho
hhcho@yonsei.ac.kr

[1] Department of Mechanical Engineering, Yonsei University, 50 Yonsei-ro, Seodaemun-gu, Seoul 120-749, Korea

[2] Korea District Heating Corporation, 781 Yangjae-daero, Gangnam-gu, Seoul 135-220, Korea

[3] Department of Energy System Engineering, Korea National University of Transportation, 50 Daehak-ro, Chungju-si, Chungbuk 380-702, Korea

List of symbols

d	Hole diameter
E	Young's modulus
h	Convective heat transfer coefficients, $q''/(T_w - T_{ref})$
k	Thermal conductivity
Re	Reynolds number, $\rho Ud/\mu$
T_{cool}	Temperature of coolant
T_{hot}	Temperature of combustion gas
T_{ref}	Reference temperature
T_w	Temperature of the wall

Greek symbols

σ_w	Thermo-mechanical stresses on the wall
β	Thermal expansion coefficient
μ	Viscosity
v	Poisson's ratio

1 Introduction

To improve the thermal efficiency and power output of gas turbines, a higher turbine inlet temperature is necessary. This requires advanced super-alloy materials for the gas turbine component substrates and their ceramic thermal barrier coatings. Additionally, various cooling methods, such as internal passage cooling, film cooling, and impinging jet cooling, can be applied simultaneously to minimize thermal damage to the components [1–3].

Among the gas turbine components, the combustion liner experiences excessively high thermal loads, due to its direct interaction with the combustion gas; the cooling schemes mentioned above have been applied to protect the liner. The combustion liner consists of three sections: a forward shell, a center shell, and an after shell, as shown in Fig. 1a. A different cooling method is applied to each section in an attempt

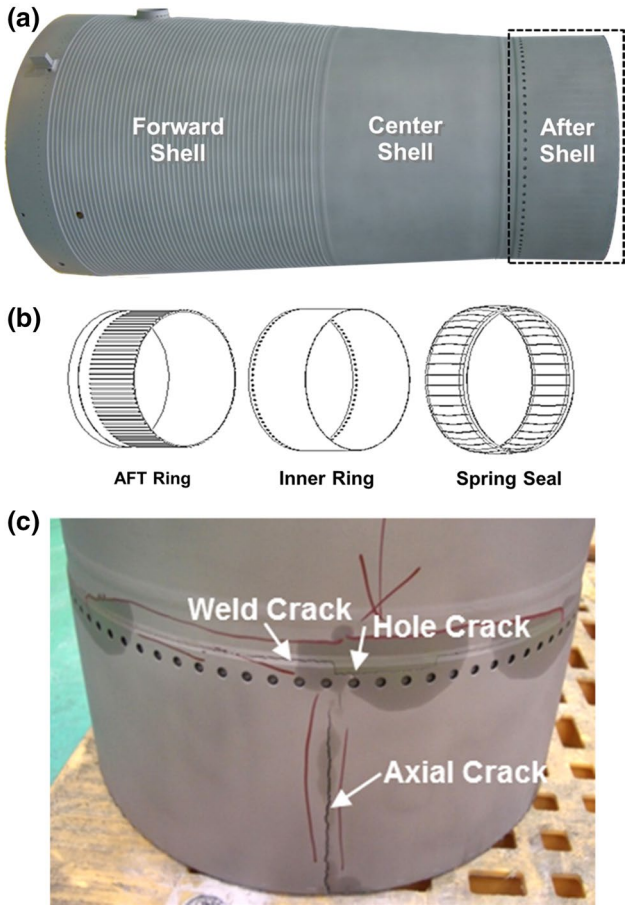

Fig. 1 Geometry of the combustion liner: **a** target combustion liner, **b** detailed assembly for the after shell, and **c** real cracks on the combustion liner after shell

to protect the entire combustion liner from excessive thermal loads. For example, rib-roughened passage cooling, impingement jet cooling, and internal passage cooling (C-channel cooling) are used to protect the forward shell, center shell, and the after shell, respectively. Among these, the after shell is exposed to the hottest combustion gas, following mixing of the gases and flow along the combustion liner. The after shell region is connected to a transition component; thus, a complex cooling structure is used to handle the higher thermal load. In practice, the after shell production requires welding of the after ring, inner ring, and spring seal, as depicted in Fig. 1b. Thermo-induced damages corresponding to crack formation in the combustion liner have been reported for gas turbine systems (Fig. 1c); thus, repair and maintenance of the combustion liner, especially the after shell assembly, remains a key issue [4, 5].

From archival journals and reports, most of the damage associated with the hot gas turbine components occurred as a result of a combination of thermal loading and mechanical impact; i.e., thermo-mechanical stress. The thermo-mechanical stress distribution for these components is strongly related to the heat transfer distribution of the cooling system. Thus, it is necessary to design a cooling system that prevents thermo-mechanical damage, as well as reduces the average temperature to below the damage threshold of the hot components. In short, the thermal design of the combustion liner cooling system should not only enhance cooling performance but also reduce the thermal stress.

Recently, advances in numerical analysis techniques via high-performance computing capabilities have facilitated more detailed analysis of the thermo-mechanical system of gas-turbine combustion components. Most of the numerical investigations to date have focused on heat transfer, temperature, and thermal stress distribution of the combustion components, with the associated lifecycle predictions. These studies have shown that conjugated heat transfer calculations are required to obtain the temperature distribution in a gas turbine combustion liner. For the prediction, thermal-flow calculations on the inside and outside of the combustion chamber were conducted to obtain the adjacent wall temperatures and heat transfer coefficients. Using these results, the temperature distribution of the entire combustion liner was predicted [6]; thermal and thermo-mechanical stress simulations were performed as part of a supplementary study [7]. Additionally, the lifetime or lifecycle of the combustion liner has been predicted using thermal/thermo-mechanical stress results, calculated using finite element method (FEM) commercial code [8–17].

In the present study, we conducted thermal design simulations in an attempt to minimize the thermo-mechanical damage of the combustion liner. Among the combustion liner components, we focused on the after shell, due to its exposure to the hottest combustion gases. Additionally, studies have shown that thermal cracks are most likely to be found in the proximity of the after-shell section, as shown in Fig. 1c [8, 9]. To minimize the thermo-mechanical damage or cracks in the after shell, we proposed three after-shell configurations: an inline-discrete divider wall array, a staggered divider wall array, and a swirler wall array; all of these structures are well-known heat-transfer enhancing structures. Finite volume method (FVM) and FEM approaches were conducted simultaneously as a conjugate problem, to compare the thermo-mechanical stress distribution for each suggested model quantitatively.

2 Problem statement

Figure 2a shows the thermo-mechanical stress distribution and real cracks on a combustion liner after shell. There are several stress-concentrated regions in the after shell, especially on the coolant side near the outer surface of the inner ring. The welded area between the AFT ring and inner ring (Fig. 1b), the cooling-hole area, and the divider wall contact area are all vulnerable to thermo-mechanical stress [8, 9]; this prediction is

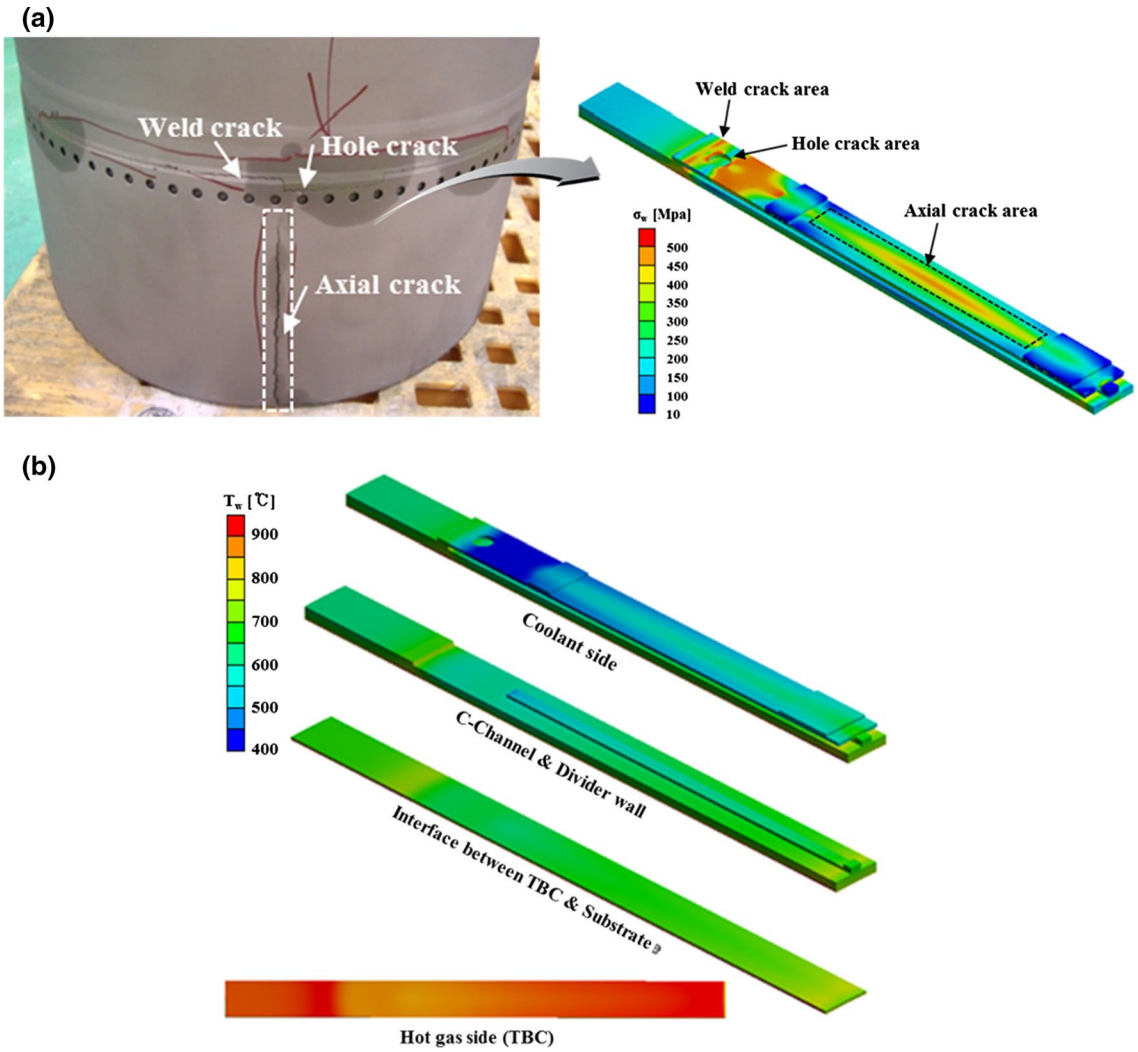

Fig. 2 **a** Thermo-mechanical stress distribution and real cracks on the combustion liner after shell and **b** the temperature distribution on the after shell

well matched to the actual cracked regions in the combustion liner, which are referred to as the weld crack, the hole crack, and the axial crack, respectively, as shown in Fig. 2a.

Figure 2b depicts the temperature distribution of the entire after shell. The welded region is exposed to large temperature differences of about 200 °C between the cooling hole area and the continuous tip area. Hence, the different thermal expansion rate concentrates the thermal stress in this region, potentially leading to weld crack formation. Additionally, the cooling-hole area is constrained by a spring seal, which tends to also concentrate the thermal stress. Near the divider wall contact, the combination of the expansion of the divider wall and the spring seal constraint induces stress formation, as shown in Fig. 2a. Thus, the uneven temperature distribution in the individual systems, resulting from variations in thermal expansion, contribute to the overall stress on the after shell assembly.

In the analysis of the thermo-mechanical characteristics and thermal damage, the damages on the after shell were due to the interaction among flow-induced thermal characteristics and structural constraints. Several design geometries were proposed in an attempt to minimize cracking in the after shell by enhancing heat transfer; specifically, an inline-discrete divider wall array, staggered divider wall array, or swirler wall array.

3 Research methods

3.1 Modeling of a single after shell and the proposed geometries

The cooling system for the after shell was designed with 88 holes along the circumference direction; these holes direct

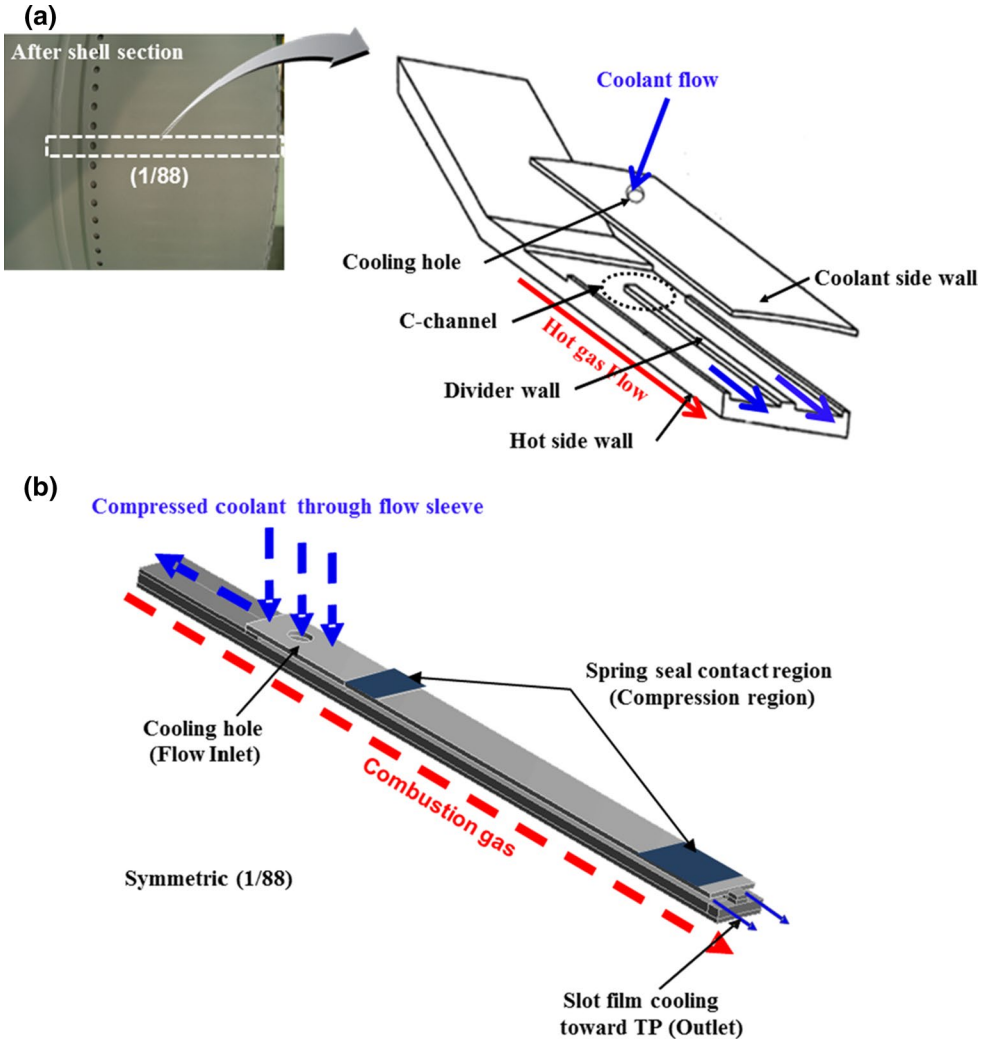

Fig. 3 Model used for thermo-mechanical analysis: **a** composition of a single after shell (1/88) and **b** the boundary conditions of the single after shell

the coolant to a small passage; i.e., a C-channel, as shown in Fig. 3a. The impinging jet cooling effect appears on the bottom plate of the C-channel. The coolant then flows through the C-channel. Because the holes and divider walls were arranged in a periodic array, one segment from the 88 cooling holes was selected for each model calculation, considering the radius of curvature of the combustion liner in its actual scale (Fig. 3b).

Three modified array models were proposed: (1) an inline-discrete wall array (a discrete divider wall with an inline array), (2) a staggered wall array (a discrete divider wall with a staggered array), and (3) a swirler wall array (a divider wall with a 45°-angle inclined array), as shown in Fig. 4a–c, respectively.

3.2 Material properties and operating conditions

The combustion liner substrate was constructed from a nickel-based super-alloy substrate (Nimonic 263). The thermal barrier coating (TBC) material, yttria-stabilized zirconia, coated the combustion liner to prevent direct interaction between the substrate and the hot combustion gases. The analysis of the temperature and stress distributions on the after shell used the constituent material properties, including the thermal conductivity (k), thermal expansion coefficient (β), Young's modulus (E), and Poisson's ratio (v), corresponding to a temperature range of 100–1000 °C for the Nimonic 263 substrate (Table 1) and from 400 to 1200 °C for the yttria-stabilized zirconia TBC material (Table 2). Among the operating modes, we considered the base-load condition for the calculations. During a gas turbine operation cycle, the firing temperature under base-load conditions is the highest (~1350 °C); thus, we considered steady-state base-load conditions for the calculations [9].

3.3 Fluid flow and heat transfer analysis

To investigate the fluid flow and heat transfer of each model, three-dimensional (3-D) analysis was performed using the commercial code Fluent v6.3. The governing

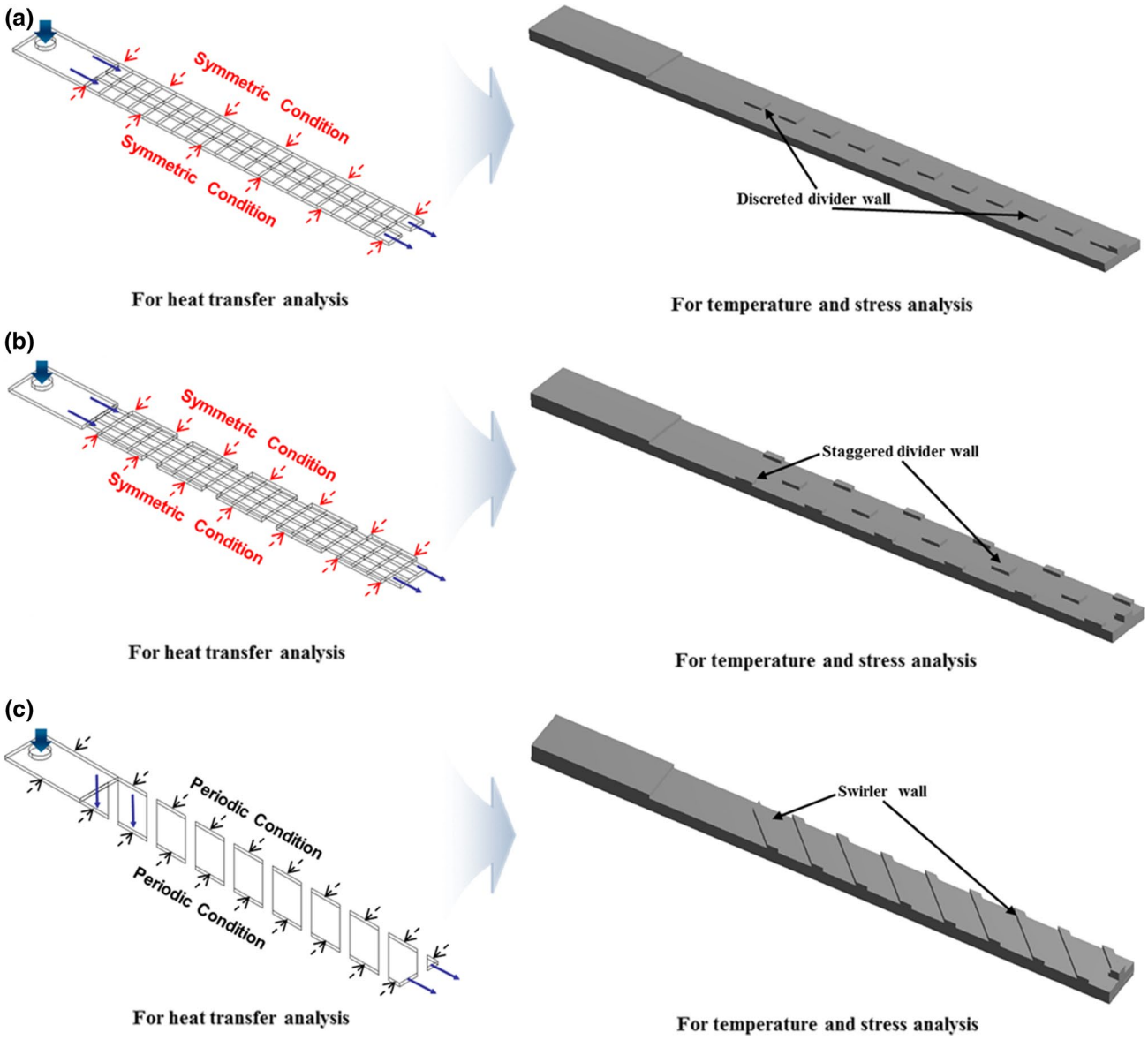

Fig. 4 Geometry of the proposed models: **a** discrete divider wall with inline array, **b** discrete divider wall with staggered array, and **c** a divider wall with a 45° angle inclined array

Table 1 Physical properties of the super-alloy (Nimonic 263) [8, 9, 18]

Temperature (°C)	Thermal conductivity (W/m-°C)	Thermal expansion coefficient (μm/m-°C)	Young's modulus (GPa)	Poisson's ratio
100	13.0	11.0	217	0.382
200	14.7	12.1	212	0.384
400	18.0	13.0	198	0.387
600	21.4	13.9	185	0.391
800	24.7	15.3	168	0.397
1000	28.5	17.4	143	0.402

equations were solved with appropriately confined boundary conditions. The inlet conditions of the coolant were set to a flow temperature of 400 °C and a pressure of 15 bar, in detail, the fluid is assumed to be incompressible with constant thermal physical properties at actual coolant temperature and pressure condition (dry air @ 400 °C and 15 bar).

Table 2 Physical properties of the yttria-stabilized zirconia thermal barrier coating (TBC) [8, 9, 18]

Temperature (°C)	Thermal conductivity (W/m °C)	Thermal expansion coefficient (μm/m-°C)	Young's modulus (GPa)	Poisson's ratio
400	2.1	10.2	30.5	0.265
600	2.13	10.3	31.3	0.268
800	2.2	10.4	32.0	0.270
1000	2.3	10.5	32.5	0.275
1100	2.35	10.4	31.3	0.278
1200	2.4	10.3	30.1	0.280

Table 3 Grid independence test

	Grid 1 (1,590,636)	Grid 2 (4,082,290)	Grid 3 (6,169,990)
h_{avg} (W/m^2 K)	1465.9862	1617.467	1616.917

A flow-entrance velocity of 34.77 m/s (Reynolds number of 40,000), and a turbulence intensity of 3 % were also set. A constant heat flux condition was assumed for the channel surface.

The velocity and pressure were solved using the semi-implicit method for pressure-linked equations (SIMPLE) pressure-correction algorithm. The coolant fluid was assumed to be incompressible, and the fluid properties were assumed to be constant. The renormalization group (RNG) k-ε model was chosen as the turbulence model [19–24], and standard wall functions were applied at the walls as a near-wall treatment, along with y^+ values ranging from 10 to 30 [19, 21–23]. Moreover, on each side of the flow path, symmetric boundary conditions were used; periodic boundary conditions were determined only for the swirler wall array design. The geometry and grid were generated by the commercial code GAMBIT v2.3. In each section, unstructured, multi-block grids were built using similar grid numbers (approximately 4 million) for each model, and grid independence tests were performed. Three grid systems, consisting of 1,590,636, 4,082,290, and 6,169,990 cells, were constructed [21–25]. The calculated averaged heat transfer coefficient for the channel surface from the three grid systems is listed in Table 3. From these results, 'Grid 2', consisting of 4,082,290 cells, was chosen for the study to balance the calculation time and prediction accuracy for each case.

3.4 Temperature and stress distribution analysis

FEM analysis was conducted for the temperature distribution and thermo-mechanical stress distribution using the commercial code ANSYS v.11. In the calculation, wall heat transfer data obtained from FVM calculations were used as the boundary conditions (coolant pathway). The boundary conditions of the other external surfaces; i.e., the hot combustion gas side ($h = 1000$ W/m^2 K, $T_{hot} = 1350$ °C), compressed coolant air side above the spring seal ($h = 150$ W/m^2 K, $T_{cool} = 400$ °C), and compressed coolant air side ($h = 2000$ W/m^2 K, $T_{cool} = 400$ °C), were the same as those used in our previous study [8, 9]. For the temperature and stress distribution, symmetric boundary conditions were applied at both continuous side edges (circumferential direction) of the model; a constant vertical force (1000 N) caused by the spring seal contact was determined in the reverse z-axis direction (Fig. 3b). Because we only focused on the after-shell section of the combustion liner, the mechanical coupling condition of the entire combustion liner body was applied to the surface at the end of the after shell body. Spot and continuous welding were used in the three-component assembly; thus, actual contact configurations were considered in the simulations. This required the application of a free-sliding condition between the divider wall and the inner ring contact region [26]. Otherwise, the fixed condition was applied to the welded regions, after the ring-inner ring interface and the inner ring-spring seal interface regions. The FEM mesh was generated by an ANSYS-mesh; the total number of elements and nodes were approximately 120,000 and 320,000 for each model, respectively.

4 Results and discussion

4.1 Thermo-mechanical characteristics for the inline-discrete wall array

Figure 5a shows that the heat transfer distribution along the coolant path in the after shell, using an inline-discrete divider wall array. The maximum value of the heat transfer coefficient was 3838 W/m^2 K near the stagnation point. This heat transfer coefficient is calculated by following equation in the code [19]:

$$h_{surface} = \frac{q_{surface}}{T_{suerface} - T_{ref}} \quad (1)$$

where $q_{surface}$ is heat flux on the surface, $T_{surface}$ is the local temperature on the surface of cell, and T_{ref} is the reference

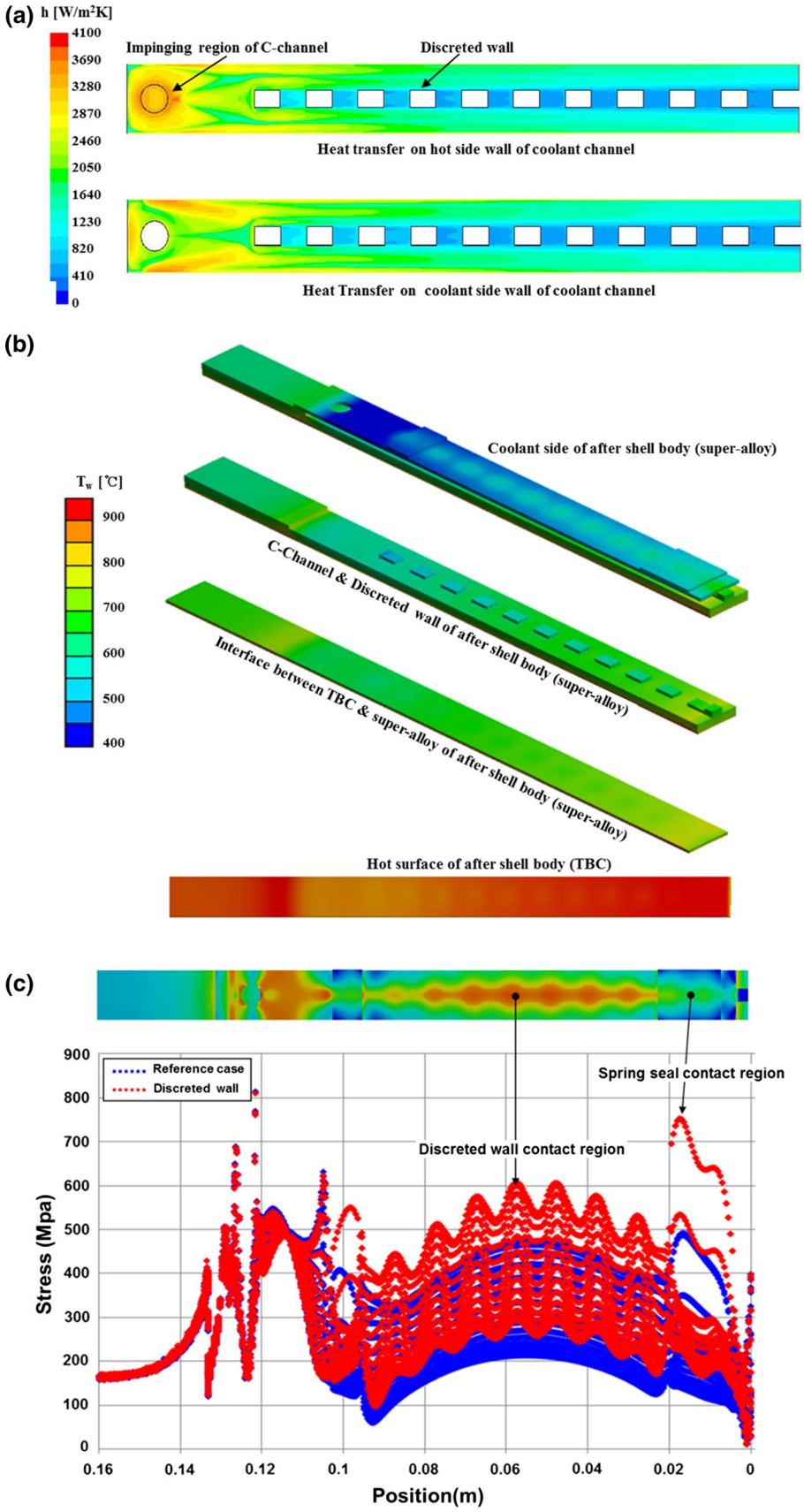

Fig. 5 Inline-discrete wall array: **a** heat transfer distribution in the coolant passage (or C-channel), **b** temperature distribution on the after shell body [the super-alloy and thermal barrier coating (TBC)], and **c** thermo-mechanical stress distribution on the after shell

temperature at the inlet of coolant. Due to the small gap between the nozzle and impinging region, the impinging flow accelerated near the stagnation point and then transitioned into a turbulent flow along the radial direction. Thus, a maximum heat transfer value appeared near the stagnation point [27, 28]. The upper side of the C-channel region (coolant side wall) exhibited a locally high heat-transfer coefficient distribution, due to the developed wall jet.

The main flow characteristic of the inline-discrete array was a steady recirculation region, which appeared behind the discrete block [29]. Due to this flow characteristic, each gap of the inline-discrete walls (i.e., the wake region) showed a low heat-transfer coefficient. Even though the wake was generated behind the trailing edge of each wall, the wake remained and recirculated; the streamwise pitch was too small for Karman vortices development. A relatively lower heat transfer coefficient was predicted for each gap of the inline-discrete walls.

Figure 5b shows the temperature distributions on the after shell with the inline-discrete divider wall. The temperature distribution ranged from 407 to 958 °C. A temperature difference between the wall gaps appeared, due to the uneven heat transfer distribution of each wall gap. The uneven temperature distribution between the gaps and the poor structural support due to a decrease in the supporting area appeared to contribute to the uneven thermal expansion of the after shell. The uneven thermal expansion affected the strain concentration between the gaps, resulting in greater stress concentration on the discrete wall contact area due to upward pushing of the inner ring. Therefore, as indicated in Fig. 5c, more concentrated stress appeared on the discrete wall contact region and spring seal contact region. Thus, to apply the inline-discrete array structure as a cooling component, the streamwise and transverse pitch of the periodic array should be optimized first.

4.2 Thermo-mechanical characteristics of the staggered wall array

Figure 6a shows the heat transfer distribution along the coolant pathway of the after shell for the staggered wall array. Near the impinging region of the C-channel, the heat transfer distribution was similar to that of the inline-discrete array, due to the same geometry of the impinging region. However, the maximum heat transfer value (4062 W/m^2 K) appeared at the beginning of the staggered wall, due to the flow impingement and acceleration in this region. However, for the wake region of each wall, the flow was blocked by both walls streamwise, allowing for acceleration and shedding of the flow [29–31]. Due to continuous coolant acceleration and shedding, the overall heat transfer distribution increased, compared with the inline-discrete wall array.

Figure 6b shows the temperature distribution for the staggered wall array. The temperature varied from 406 to 933 °C. Compared with the inline-discrete wall array, the maximum temperature, which appeared on the TBC, was smaller. The average heat transfer coefficient increased in the staggered array region (the coolant region); thus, a relatively lower temperature appeared in the hot gas region.

Figure 6c shows the thermo-mechanical stress distribution on the inner ring. The staggered wall contact region indicated a lower stress distribution compared with the reference case. This is because the enhancement of the cooling effect on the staggered wall region reduced the thermal expansion to the inner ring. However, in the proximity of the spring seal contact, a relatively high stress distribution appeared, due to the diminished supporting area on this constraint region.

4.3 Thermo-mechanical characteristics of the swirler wall array

Figures 7a, b show the heat transfer distribution and path lines of the impinging region of the C-channel with a swirler wall array. The maximum value of the heat transfer coefficient was 3868 W/m^2 K near the first swirler wall region. This is because the impinging flow was turned rapidly by the first swirler wall, which had an incline of 45°. At the back side of each swirler wall, the heat transfer was relatively low, due to the separation and reattachment of the coolant near the back side of the wall as the flow developed.

Figure 7c indicates the temperature distribution on the after shell body with the swirler wall array. The temperature distributions ranged from 406 to 943 °C. Although the cooling effect differed only slightly from the reference case, the swirler wall can function closer to a radiant fin, compared with the other models, having an enhanced coolant contact area.

Figure 7d depicts the thermo-mechanical stress distribution on the inner ring. In the swirler wall contact area (the inner ring proximity), the stress distribution was lower and appeared to be uniform. Additionally, the stress distribution on the spring seal contact region was similar to that of the reference case. Thus, a slight increase in the cooling capacity and the supporting area better distributed the thermo-mechanical stress.

4.4 Comparison of the thermo-mechanical characteristics among designs

Table 4 shows the temperature distribution range of the entire after shell, and the maximum stress on the wall contact region and spring seal contact region. From the temperature distribution results, the heat-transfer-enhanced arrays; i.e., the staggered wall and swirler wall arrays, exhibited a

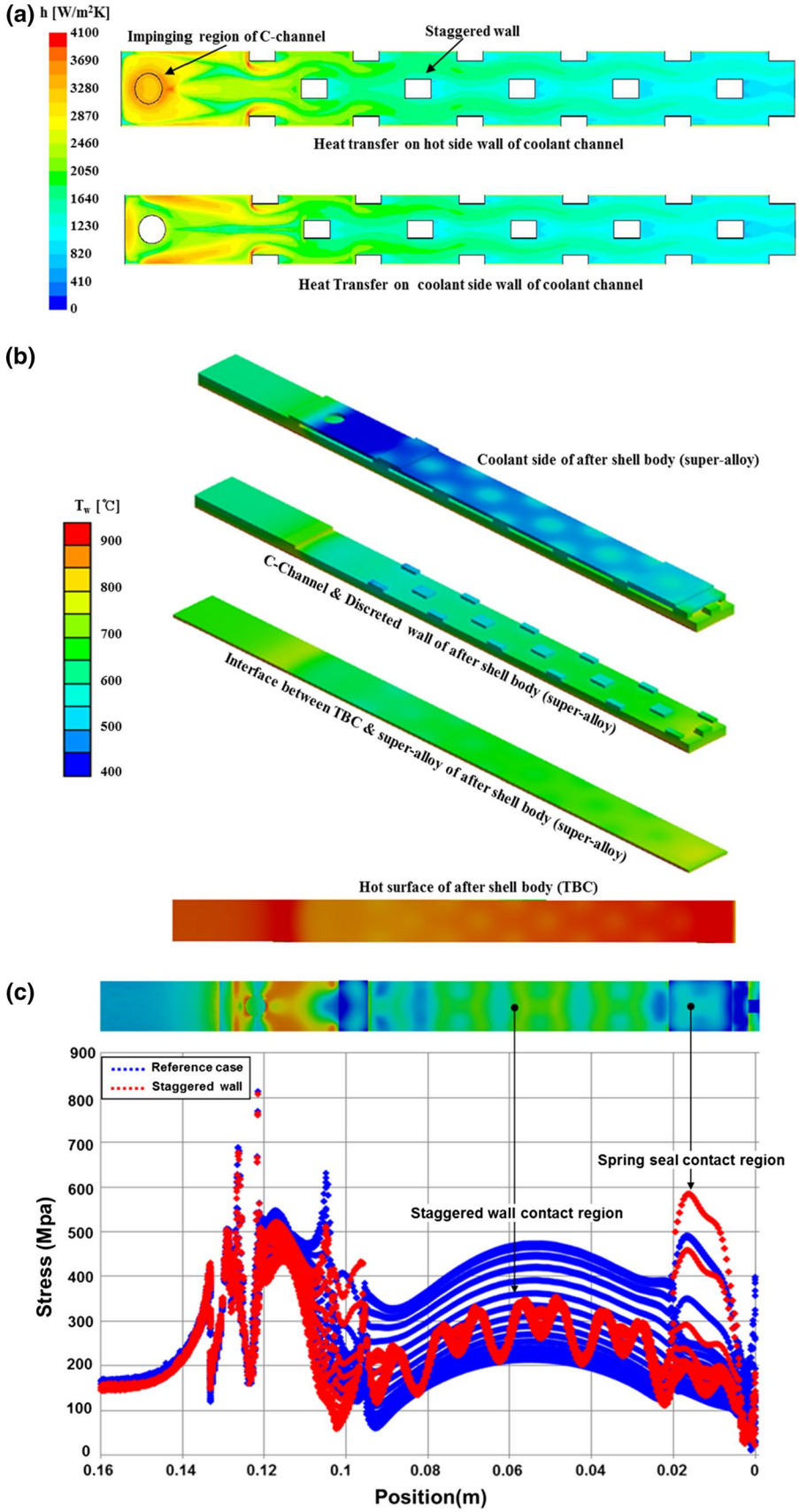

Fig. 6 Staggered wall array: **a** heat transfer distribution in the coolant passage (C-channel), **b** temperature distribution on the after shell body (super-alloy and TBC), and **c** the thermo-mechanical stress distribution on the after shell

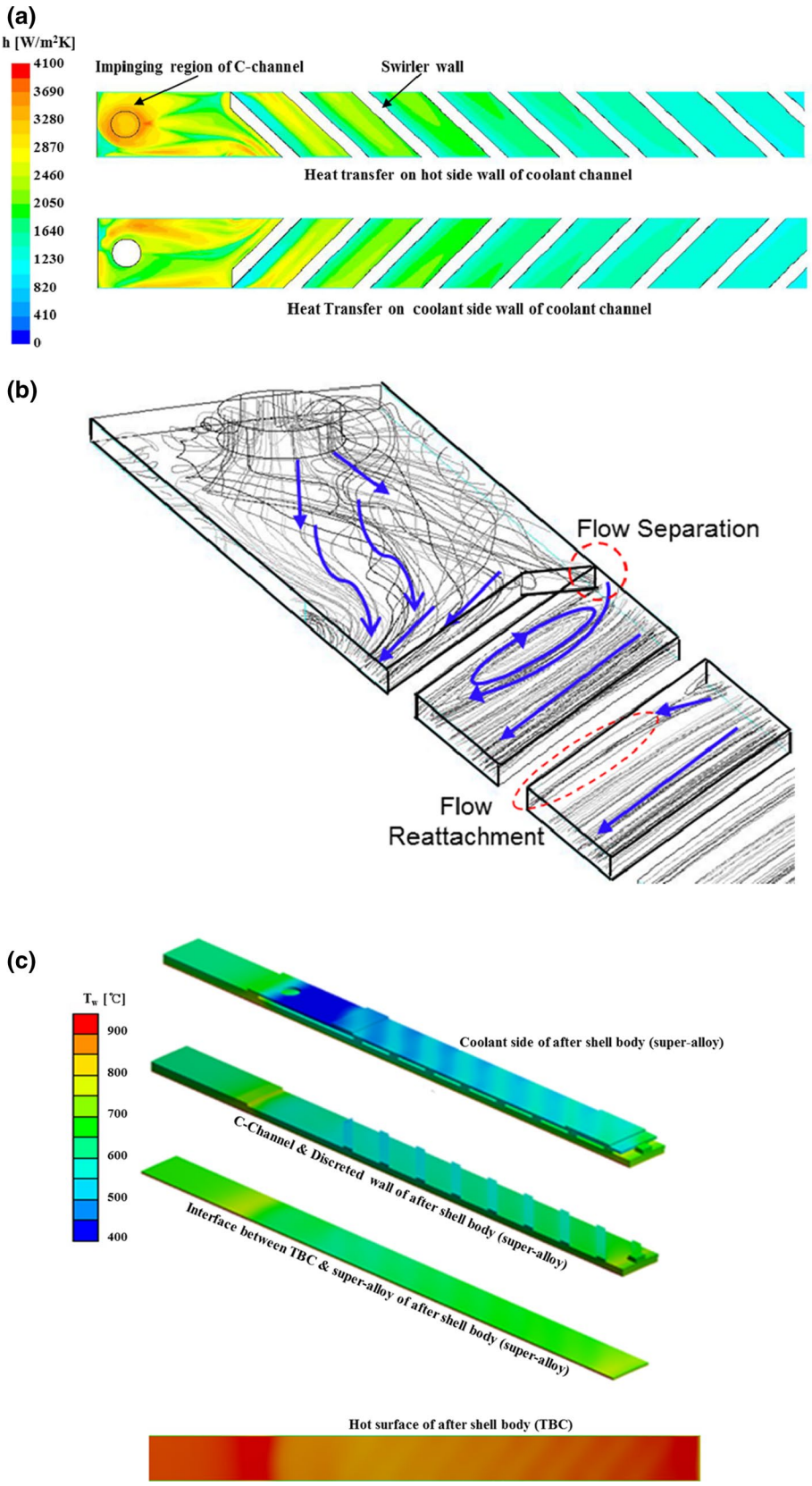

Fig. 7 Swirler wall array: **a** heat transfer distribution in the coolant passage (C-channel), **b** path line of the coolant passage (around the jet impingement region), **c** temperature distribution on the after shell body (super-alloy and TBC), and **d** the thermo-mechanical stress distribution on the after shell

Fig. 7 continued

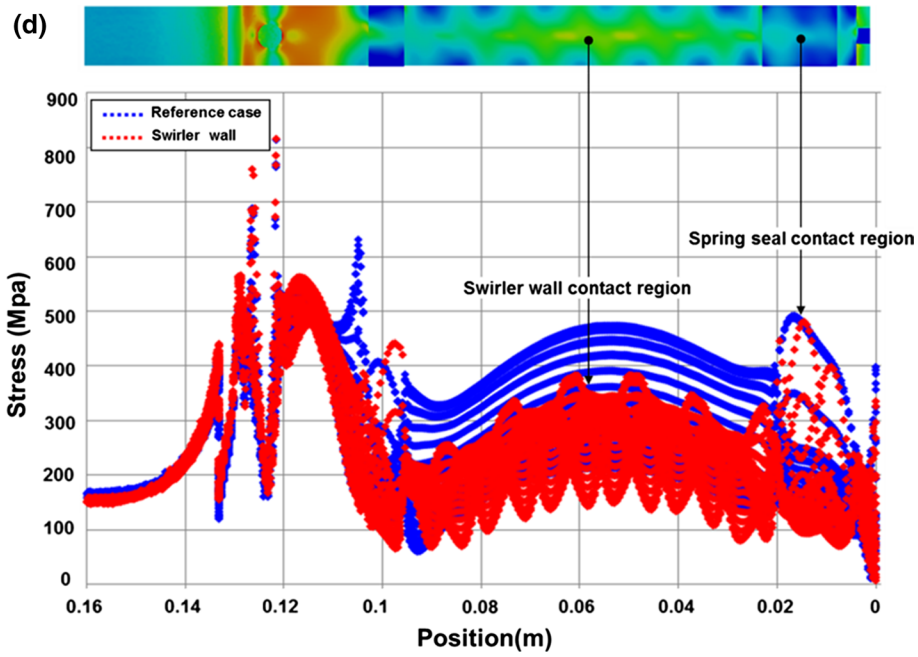

Table 4 Temperature and stress distribution range of the entire after shell

Wall arrays	Range of after shell temperature distribution (°C)	Maximum stress on wall contact region (MPa)	Maximum stress on spring seal contact region (MPa)
Divider wall (referecne case)	407–953	450	500
Inlined-discreted wall	407–958	610	750
Staggered wall	406–933	370	590
Swirler wall	406–943	390	490

higher cooling capacity. This enhancement in cooling corresponded to a reduction in the thermal stress concentration on the staggered wall contact region (Fig. 6c) and the swirler wall contact region (Fig. 7d). The enhanced, even cooling capacity reduced thermal expansion, resulting in an upward force on the inner ring. Additionally, the swirler wall array was shown to be effective in thermal stress reduction, compared with the other proposed cases; this was attributed to the greater supporting area of this array configuration.

Thus, among the proposed design schemes, the swirler wall array was the most effective in reducing the likelihood of thermo-mechanical crack formation on the inner ring. Our results also emphasize the importance of considering the structural support characteristics for a more thermally robust design.

5 Conclusions

In this study, thermo-mechanical analysis was conducted on several after shell configurations in an attempt to reduce thermo-mechanical damage in a gas turbine combustion liner. Three cooling design structures were tested for the after shell: an inline-discrete divider wall, staggered divider wall, and swirler wall; these structures have demonstrated enhanced heat transfer. Three-dimensional (3-D) numerical analyses were conducted using Fluent and ANSYS commercial codes to predict the coolant flow pattern, heat transfer, temperature, and thermo-mechanical stress distribution for each of the three models. From thermal damage analysis, three regions were identified as having a high stress concentration: the weld site, cooling-hole site, and divider wall contact area site. The predicted damage areas were in good agreement with the cracked regions observed on the combustion liner upon examination. The heat transfer distribution and heat transfer values were similar to those corresponding to the impinging region of the C-channel (with slight dissimilarities for the swirler wall case). The staggered walls and the swirler walls were especially effective in cooling the liner, thereby enhancing heat transfer and increasing the radiant area, as evidenced by the temperature distribution over the entire shell. Although the inline array generally exhibited unique flow characteristics for heat

transfer enhancement, optimization should be considered with the streamwise and transverse pitch of the periodic arrays. Comparing the thermo-mechanical stress distributions, the heat transfer enhancing array (staggered) and the radiant/supporting area increasing array (swirler) show a significant reduction in the thermo-mechanical stress on the inner ring. However, when considering the structural supporting area, especially the spring seal contact region, the swirler wall array was the better choice for adaptation to the after shell assembly. Finally, the thermal design for the cooling system should consider not only the cooling capacity but also the temperature uniformity of the system.

Acknowledgments This work was supported by the 'Human Resources Development program (No. 20144030200560)' of the Korean Institute of Energy Technology Evaluation and Planning (KETEP) grant funded by the Korean government Ministry of Trade. This work was also supported by the 'Power Generation & Electricity Delivery (No. 2014101010187A)' of the Korea Institute of Energy Technology Evaluation and Planning (KETEP). This program is funded by the Korean government Ministry of Trade, Industry and Energy.

References

1. Goldstein RJ (1971) Film cooling. Adv Heat Transf 7:321–379
2. Lakshminarayana B (1996) Frontmatter. Wiley Online Library, New Jersey
3. Han J-C, Datta S, Ekkad S (2013) Gas turbine heat transfer and cooling technology. CRC Press, Florida
4. Grace D (2007) Design evolution, durability and reliability of mitsubishi heavy industries heavy duty combustion turbines. Electric Power Research Institute, Palo Alto
5. Grace D (2007) Design evolution, durability and reliability of general electric heavy duty combustion turbines. Electric Power Research Institute, Palo Alto
6. Kim KM, Yun N, Jeon YH, Lee DH, Cho HH, Kang S-H (2010) Conjugated heat transfer and temperature distributions in a gas turbine combustion liner under base-load operation. J Mech Sci Technol 24:1939–1946
7. Tinga T, Jv Kampen, Jager Bd, Kok J (2007) Gas turbine combustor liner life assessment using a combined fluid/structural approach. J Eng Gas Turbines Power 129:69–79
8. Kim KM, Yun N, Jeon YH, Lee DH, Cho HH (2010) Failure analysis in after shell section of gas turbine combustion liner under base-load operation. Eng Fail Anal 17:848–856
9. Kim KM, Jeon YH, Yun N, Lee DH, Cho HH (2011) Thermo-mechanical life prediction for material lifetime improvement of an internal cooling system in a combustion liner. Energy 36:942–949
10. Kim KM, Lee DH, Cho HH (2010) Lifetime prediction of film cooling systems with and without thermal barrier coating. Int J Fluid Mach Syst 3:181–187
11. Zhai J, Zhou M (2000) Finite element analysis of micromechanical failure modes in a heterogeneous ceramic material system. Int J Fract 101:161–180
12. Cunha F, Dahmer M, Chyu M (2006) Thermal-mechanical life prediction system for anisotropic turbine components. J Turbomach 128:240–250
13. Kim KM, Park JS, Lee DH, Lee TW, Cho HH (2011) Analysis of conjugated heat transfer, stress and failure in a gas turbine blade with circular cooling passages. Eng Fail Anal 18:1212–1222
14. Kim KM, Shin S, Lee DH, Cho HH (2011) Influence of material properties on temperature and thermal stress of thermal barrier coating near a normal cooling hole. Int J Heat Mass Transf 54:5192–5199
15. Mazur Z, Hernández-Rossette A, García-Illescas R, Luna-Ramírez A (2006) Analysis of conjugate heat transfer of a gas turbine first stage nozzle. Appl Therm Eng 26:1796–1806
16. Y-j Xie, M-c Wang, Zhang G, Chang M (2006) Analysis of superalloy turbine blade tip cracking during service. Eng Fail Anal 13:1429–1436
17. Moon H, Kim KM, Jeon YH, Shin S, Park JS, Cho HH (2015) Effect of thermal stress on creep lifetime for a gas turbine combustion liner. Eng Fail Anal 47:34–40
18. Special Metal Corporation (2007) Special metals product hand book of high-performance alloys [Publication No. SMC-054]
19. Fluent F (2006) 6.3 user's guide. Fluent Inc
20. Zuckerman N, Lior N (2006) Jet impingement heat transfer: physics, correlations, and numerical modeling. Adv Heat Transf 39:565–631
21. Xie G, Sundén B, Wang L, Utriainen E (2009) Enhanced internal heat transfer on the tip-wall in a rectangular two-pass channel (AR = 1: 2) by pin-fin arrays. Numer Heat Transf Part A: Appl 55:739–761
22. Xie G, Sundén B, Utriainen E, Wang L (2010) Computational analysis of pin-fin arrays effects on internal heat transfer enhancement of a blade tip wall. J Heat Transf 132:031901
23. Xie G, Sundén B, Zhang W (2011) Comparisons of pins/dimples/protrusions cooling concepts for a turbine blade tip-wall at high Reynolds numbers. J Heat Transf 133:061902
24. Fasquelle A, Pellé J, Harmand S, Shevchuk IV (2014) Numerical study of convective heat transfer enhancement in a pipe rotating around a parallel axis. J Heat Transf 136:051901
25. Shevchuk IV, Jenkins SC, Weigand B, von Wolfersdorf J, Neumann SO, Schnieder M (2011) Validation and analysis of numerical results for a varying aspect ratio two-pass internal cooling channel. J Heat Transf 133:051701
26. ANSYS Inc (2008) ANSYS user's guide
27. Lytle D, Webb B (1994) Air jet impingement heat transfer at low nozzle-plate spacings. Int J Heat Mass Transf 37:1687–1697
28. Cho HH, Rhee DH (2001) Local heat/mass transfer measurement on the effusion plate in impingement/effusion cooling systems. J Turbomach 123:601–608
29. Balachandar S, Parker S (2002) Onset of vortex shedding in an inline and staggered array of rectangular cylinders. Phys Fluids 14:3714
30. Tanda G (2001) Heat transfer and pressure drop in a rectangular channel with diamond-shaped elements. Int J Heat Mass Transf 44:3529–3541
31. Park JS, Chyu M, Kim KM, Lee DH, Cho HH (2011) Heat transfer in rotating channel with inclined pin-fins. J Turbomach 133:021003